Ultrathin sulfur-doped holey carbon nitride nanosheets with superior photocatalytic hydrogen production from water

Lei Luo[a], Zhuyu Gong[a], Jiani Ma[a]*, Keran Wang[a], Haixing Zhu[a], Keyan Li[b], Lunqiao Xiong[c],

Xinwen Guo[b]*, Junwang Tang[c]*

[a] Key Lab of Synthetic and Natural Functional Molecule Chemistry of Ministry of Education, the

Energy and Catalysis Hub, College of Chemistry and Materials Science, Northwest University,

Xi'an 710127, P. R. China.

[b] State Key Laboratory of Fine Chemicals, PSU-DUT Joint Center for Energy Research, School of

Chemical Engineering, Dalian University of Technology, Dalian 116024, P. R. China.

[c] Department of Chemical Engineering, University College London, Torrington Place, London

WC1E 7JE, UK.

Abstract

14

15   Surface engineering is an efficient way to enhance photoabsorption, promote charge separation and

16   boost photocatalysis. Herein, sulfur-doped holey g-C_3N_4 nanosheets have been prepared through a

17   universal self-templating approach with thiocyanuric acid as the single-precursor. By subtly

18   controlling the feeding amount of precursor, the synthesized sulfur-doped holey g-C_3N_4 nanosheets

19   exhibit excellent visible-light driven photocatalytic hydrogen production activity. The optimized

20   catalyst presents a hydrogen evolution rate of 6225.4 $\mu mol \cdot g^{-1} \cdot h^{-1}$, with an apparent quantum yield of

21   10 % at 420 nm. Comprehensive characterizations and theoretical calculations suggest that the

22   enhanced photocatalysis is attributed to the synergy of the enlarged surface area, the negatively-

23   shifted conduction band, and the narrowed bandgap due to sulfur-doping and ultra-thin two-

24   dimensional topology. This work highlights the importance of controlling the precursor dosage and

25   inducing sulfur doping into the polymer, providing a promising and reliable strategy to

26   simultaneously regulate the nanostructural and electronic structure of g-C_3N_4 for highly efficient

27   photocatalysis.

28

29   *Keywords:* graphitic carbon nitride; surface modification; sulfur-doping; two-dimensional materials;

30   visible water splitting

31

1. Introduction

Highly efficient photocatalysts have attracted tremendous attention due to their potential applications in renewable energy supply and environmental remediation [1-3]. The key is the development of efficient photocatalysts. Among various photocatalysts, graphitic carbon nitride (g-C_3N_4) has emerged as a promising metal-free visible-light responsive photocatalyst due to its moderate bandgap and high stability [4-6]. Thermolysis of various nitrogen-rich precursors could prepare g-C_3N_4 in large-scale, but the insufficient photoabsorption, high charge recombination rate and low quantum yield still suppress its photocatalytic performance [7-9]. To improve the efficiency, great efforts including nanostructural and surface modification have been devoted [10-15].

Two-dimensional nanosheets are a novel category of nanostructural materials and prevailing because of their unique layered features of intriguing surface, optical and electronic properties [16-18]. Exfoliation of the bulk was a post-synthetic method to break down the interlayer van der Waals' forces into two-dimensional nanosheets, which had been demonstrated as an efficient route for shortening the charge transfer pathway, increasing the surface area and providing more active sites [19, 20]. Through ultrasonic-, thermal- and chemical-assisted exfoliation, pristine g-C_3N_4 nanosheets were prepared [19, 21, 22]. However, the enlarged surface area would result in an increased bandgap energy due to the quantum confinement effect, decreasing the photoabsorption ability. Moreover, the severe charge recombination could hardly be suppressed through simple morphological modification [23]. Therefore, developing a green and reliable strategy for low-cost assembly of two-dimensional g-C_3N_4 nanosheets as well as optimizing its electronic structure is still highly desired.

Anion doping is generally an alternative and important approach owing to the effectiveness in regulating the electronic structure and broadening the region of light absorption. With anion doping like B, O, C, P, I, the atomic and electronic properties could be positively optimized through the

injection of localized states from dopants [24-31]. As the conduction and valence band of g-C$_3$N$_4$ were theoretically confirmed to be primarily derived from the p_z orbitals of carbon and nitrogen [32], the substitution of these atoms would primarily lead to the delocalization of big π-conjugated system, boosting the conductivity of g-C$_3$N$_4$. The more negative conduction band would exhibit stronger photoreduction ability and provide stronger driving force for hydrogen evolution. Nevertheless, heteroatom dopants might also cause doping asymmetry and serve as new charge recombination sites [33, 34]. Thus, to enhance the charge separation and maintain suitable photoabsorption, subtle regulation of the type and location of dopants is of great significance.

In this work, sulfur-doped holey g-C$_3$N$_4$ nanosheets were fabricated through a controllable self-templating approach without any additives. Based on the nucleation-growth mechanism, tuning the amount of precursor would result in the optimized concentration in a semi-closed synthesis system for thermally-driven polymerization, thereafter generating g-C$_3$N$_4$ nanosheets. With thiocyanuric acid as the precursor, ultrathin sulfur-doped holey nanosheets were prepared. The dramatically enhanced photoactivity for hydrogen production is attributed to the enlarged surface area, the enhanced photoabsorption, and the suppressed charge recombination derived from the synergy of sulfur-doping and ultrathin holey nanosheet topology.

2. Experimental

2.1. Preparation of the sulfur-doped holey g-C$_3$N$_4$ nanosheets

Sulfur-doped holey g-C$_3$N$_4$ nanosheets (labelled as S-CN(x), where x represents the amount of the precursor) were prepared through one-step thermolysis of thiocyanuric acid. Various feeding amount of thiocyanuric acid from 0.1 to 2.0 g first spread in a crucible, coated with silver paper and covered with a lid. Then the semi-closed crucible was transferred to the tube furnace and underwent

calcination in the flowing argon atmosphere (99.999%) at 550 °C for 3 h at a ramping rate of 10

°C/min. After cooling down, the yellow powder was obtained. For comparison, the pristine bulk and

nanosheet g-C$_3$N$_4$ were prepared with the widely reported precursors dicyandiamide and urea under

identical condition, respectively. The samples prepared with dicyandiamide as the precursor was

denoted as D-CN, and that with urea as U-CN.

2.2. g-C$_3$N$_4$ without S-doping prepared from other common precursors

Melamine, dicyanamide, thiourea and urea were used as the precursors to investigate the universal

influence of the feeding amount on the morphology and the specific surface area. Different amount

of single precursor was calcinated under the same condition as mentioned above. The as-obtained

samples were denoted as M-CN(x), D-CN(x), T-CN(x) and U-CN(x), respectively, where x represents

the corresponding amount of the precursors.

2.3. Characterization

High-resolution transmission electron microscope (HRTEM) images were recorded on the Talos

F200X instrument (*FEI Co., Ltd*). Nitrogen physical adsorption-desorption isotherms were measured

on a TR2 Star3020 gas adsorption analyzer at 77 K. Before each measurement, the samples were

degassed at 150 °C for 8 h and backfilled with ultrapure nitrogen. X-ray diffraction (XRD) patterns

were recorded on the D8 ADVANCE diffractometer (*Bruker Co., Ltd*). X-ray photoelectron

spectroscopy (XPS) spectra were recorded on the PHI 5000 VersaProbeIII instrument (*ULVAC-PHI*

Co., Ltd). UV-Vis diffuse reflectance spectra (UV-DRS) were taken on a UV-3600 Plus spectrometer

with BaSO$_4$ as the reference. Steady-state fluorescence (PL) spectra were acquired on a JASCO FP-

6200 spectrofluorometer with the excitation wavelength at 310 nm. Time-resolved PL spectra were

collected on FLSP920 spectrofluorometer. Atomic Force Microscope (AFM) were conducted on the

Dimension ICON instrument (*Bruker Co., Ltd*). Photoelectrochemical properties were measured in a

101 conventional three-electrode cell on the CHI660E workstation with g-C$_3$N$_4$ loaded ITO glass as the

102 working electrode, Ag/AgCl as the reference electrode, platinum plate as the counter electrode and

103 Na$_2$SO$_4$ solution (0.1 M) as the electrolyte.

104 2.4. Photocatalytic hydrogen production

105 Photocatalytic water splitting for hydrogen production was performed in a Pyrex top-irradiation

106 system equipped with a 300 W Xenon lamp ($\lambda > 420$ nm) (*PLS-SXE300D, Beijing Perfectlight*

107 *Technology Co., Ltd*) as the visible-light source. Triethanolamine (TEOA) was used as sacrificial

108 agent and platinum (Pt) as the co-catalyst. In a typical experiment, 50 mg catalyst was dispersed and

109 stirred in a 200 mL TEOA aqueous solution (10 vol.%) and 3.0 wt.% Pt was in-situ photodeposited.

110 The complete removal of air in the system was realized through continuous purging with ultrapure

111 argon (99.999%) for more than one hour before irradiation. Gaseous products were detected by the

112 3420A gas chromatograph (*Beifen Ruili Co., Ltd*) with a thermal conductivity detector. The apparent

113 quantum yield (AQY) was measured with 0.1 g photocatalysts under monochromatic light and

114 calculated by the followed equation.

$$115 \quad \mathrm{AQY}(\%) = \frac{2 \times \text{amount of H}_2 \text{ molecules evolved}}{\text{number of incident photons}} = \frac{2 \times n \times N_A}{\dfrac{E_{total}}{E_{photon}}} \times 100\%$$

$$116 \quad = \frac{2 \times n \times N_A}{\dfrac{S \times P \times t}{h \times \dfrac{c}{\lambda}}} \times 100\% = \frac{2 \times n \times N_A \times h \times c}{S \times P \times t \times \lambda} \times 100\%$$

117 Where, n represents the amount of evolved H$_2$ molecules (herein 130.5 μmol), N$_A$ is the Avogadro

118 constant (6.022×10^{23} mol^{-1}), h means the Planck constant (6.626×10^{-34} J·s), c is the light speed (3×10^8

119 m/s), S represents the irradiation area (herein 3.14 cm^2), P is the intensity of irradiation light (here in

120 65 mW·cm^{-2}), t refers to the photoreaction time (3600 s), λ represents the wavelength of the

121 monochromatic light (such as 420 nm).

3. Results and discussion

3.1. Structure and morphology

Thiocyanuric acid was used here as a sulfur-rich precursor for sulfur doped CN (S-CN) fabrication. Based on the gas-phase nucleation growth mechanism [35], decreasing the gaseous concentration could slow down the corresponding nucleation and growth rate, then being favorable for explosive nucleation, forming more crystal nucleus and getting decreased size. The concentration of the gaseous thiocyanuric acid precursor in this work was optimized through subtly controlling its feeding amount in the semi-closed system as illustrated in **Figure 1a**. Thiocyanuric acid underwent successively polymerization with temperature rising, accompanied with the weight loss from de-amino and sublimation process. If this polymerization only occurred in solid-state, the weight loss percentage would be identical no matter how much dosage of the solid precursor was used. To investigate whether the gas-phase polymerization involved, thermogravimetric analysis (TGA) was performed to simulate the thermolysis synthetic condition with varied amount of thiocyanuric acid. **Figure S1** shows the TGA curves of thiocyanuric acid with varied dose decreased from 28.79 to 5.90 mg. The dramatically different weight loss behavior clearly objects to the above hypothesis and suggests the existence of gas-phase polymerization. The weight loss below 200 $^{\circ}$C is attributed to the absorbed water, and the two samples exhibit almost the same weight loss of 2.0 wt.%, suggesting the uniform moisture content of the as-purchased thiocyanuric acid. As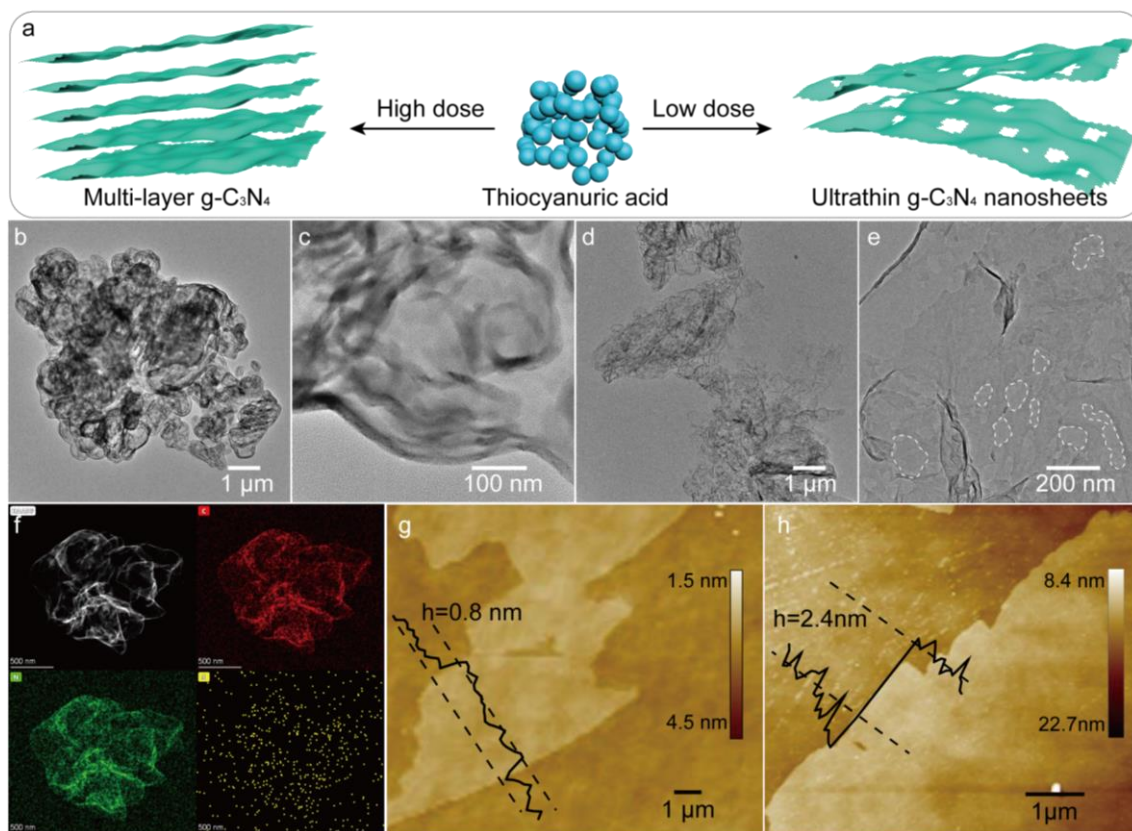 the polymerization is not a simple solid phase process, but also happens in gas-phase, which provides the basis for controlling the concentration of the polymerization system. The weight loss above 200 $^{\circ}$C is assigned to the synergy of sublimation and polymerization. As the volatilization surface of the precursors with different amount remains

145   unchanged, the rate of sublimation should be constant, thus suggesting that the weight loss from

146   polymerization primarily determines the above differences above 200 $^{\circ}$C. Under 550 $^{\circ}$C, it is clear

147   that the higher feeding amount of thiocyanuric acid during TGA experiments yields 16.4 wt.%, much

148   higher than the less feeding amount (yields 10.3 wt.%) (**Figure S1**), suggesting the higher feeding

149   amount is more conducive to polymerize and yield more. Based on the molecular collision theory

150   [35], higher concentration is more favorable to react and thereafter slows down the weight loss. As a

151   result, the higher feeding amount exhibited an obvious hysteretic weight loss about 40 $^{\circ}$C. Therefore,

152   the polymerization of thiocyanuric acid existed gas-phase polymerization and the concentration of

153   the vaporized precursor could be regulated through controlling the feeding amount in the semi-closed

154   system. To conclude, it would be feasible to tailor the morphology and surface area of g-C_3N_4 through

155   facilely controlling the feeding amount.

156

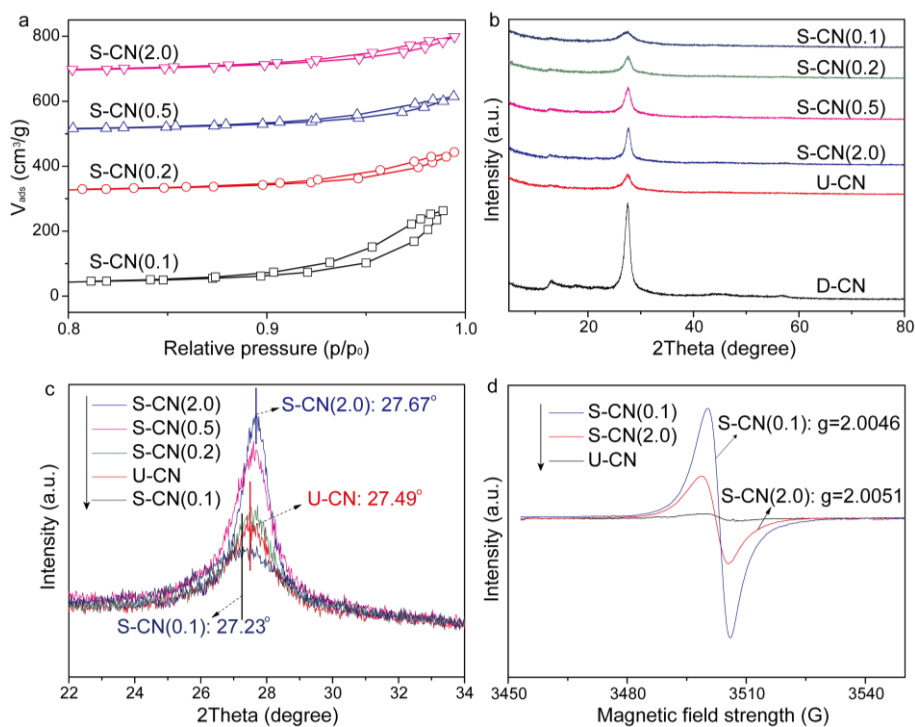
157

158   Figure 1. (a) Schematic illustration of sample preparation. HRTEM images of (b, c) S-CN(2.0) and

(d, e) S-CN(0.1). (f) TEM-mapping images of S-CN(0.1). Red, green and yellow color represent

carbon, nitrogen and sulfur elements, respectively. AFM images of (g) S-CN(0.1) and (h) S-

CN(2.0). The white circled area in (e) is the embedded hole.

The morphology of the synthesized g-C$_3$N$_4$ were observed by HRTEM and AFM. Both S-CN(2.0) and S-CN(0.1) feature the distinct nanosheet structure (**Figure 1b-e**) caused by the considerable gaseous by-products acting as the templates during polymerization into g-C$_3$N$_4$. As seen in **Figure 1b-c**, S-CN(2.0) exhibits an aggregated and curly morphology due to high concentration caused over-condensation. As a comparison, along the in-plane direction of nanosheets, S-CN(0.1) with lower degree of polymerization would perform less in-plane connections and evolve into loose and spread thin layer as evidenced by **Figure 1d-e** and **Figure S2**. More importantly, the nanosheets of S-CN(0.1) insert with numerous mesopores ranging from 30 nm to 150 nm. This is mainly due to the low polymerization concentration, which could not fulfill the long-range polymerization. While in the vertical direction of nanosheet, S-CN(0.1) performs an average of 0.8 nm thickness (**Figure 1g**), much thinner than 2.4 nm of S-CN(2.0), corresponding with approximate 3 times decrease of thickness. The minimized thickness is mainly induced by the decreased gaseous nucleation-growth rate caused by the decreased feeding amount. TEM-mapping image of S-CN(0.1) in **Figure 1f** presents the coexistence of carbon, nitrogen, and sulfur. The consistent distribution of the carbon and nitrogen elements agrees with the composition of g-C$_3$N$_4$. The observed sulfur element also exhibits the identical dispersion and might exist as the doping element and would be beneficial to regulate bandgap structure and enhance photoabsorption. Elemental analysis (**Table S1**) shows an increased sulfur content as the feeding amount decreased, i.e., S-CN(0.1) exhibits 0.26 wt.% sulfur content, higher than 0.15 wt.% of S-CN(2.0).

182

183

Figure 2. (a) Enlarged Nitrogen adsorption-desorption isotherms, (b) XRD and (c) expanded XRD

patterns, (d) EPR spectra of different photocatalysts.

186

Nitrogen physical adsorption-desorption isotherms were conducted to study the textural properties.

As shown in **Figure 2a** and **Figure S3**, all samples exhibit type IV adsorption isotherms,

corresponding with its layer structure. Compared with S-CN(2.0), S-CN(0.1) possesses a high

adsorption capacity under high relative pressure ($0.9 < p/p_0 < 1$), demonstrating the existence of

abundant mesopores and macropores [36]. The calculated surface area (S_{BET}) of S-CN(0.1) is 97.4

m^2/g, almost 1.4 times higher than that of S-CN(2.0) (67.8 m^2/g). The enlarged S_{BET} is consistent with

the morphological evolution to thin nanosheets. Based on the above phenomenon, we could conclude

that controllable fabrication of g-C_3N_4 nanosheets with tunable thickness could be realized by subtly

controlling the amount of precursor, which might be caused by the optimized nucleation and growth

rate during polymerization [35]. The decreased thickness and inserted mesopores would be beneficial
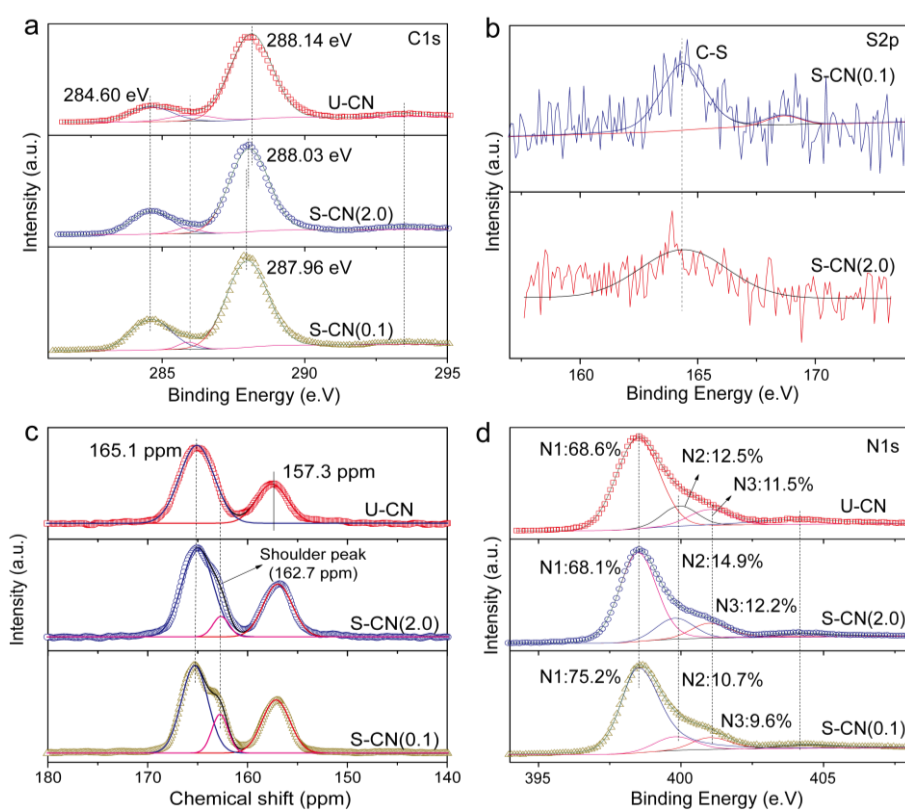
197   to shorten the charge transfer path and provide more accessible active surface.

198   The crystalline structures were determined by XRD (**Figure 2b**). For the urea-derived g-C_3N_4 (U-

199   CN), two distinguish peaks centered at 12.86º and 27.49º are characterized as the (100) and (002)

200   crystal planes of g-C_3N_4, matching with the in-plane repeated heptazine units and the stacking inter

201   layer, respectively [37]. Compared with U-CN, the (002) peak for S-CN(2.0) exhibits a right-shift

202   from 27.49º to 27.67º, corresponding to the interlayer spacing narrowing down from 0.324 to 0.322

203   nm. Higher degree of polymerization for thiocyanuric acid precursor when compared with urea could

204   contribute to this narrowed interlayer distance, which would be beneficial to the interlayer charge

205   transfer. [38, 39] While decreasing the amount of thiocyanuric acid, samples S-CN(x) show gradually

206   left-shift peak (002) from 27.67º to 27.23º, suggesting the enlarged interlayer distance from 0.322 to

207   0.327 nm (calculated by *2dsinθ=nλ*). This could be attributed to the increased structural disorder

208   degree and unsatisfied long-range polymerization, which is similar to the generation of the injected

209   mesopore as evidence by HRTEM. The distorted ultrathin nanosheet would suppress the interlayer

210   stacking and be beneficial to get a better photocatalytic stability. Meanwhile, S-CN(0.1) exhibits 3

211   times weaker intensity of (002) peak than S-CN(2.0), indicating less interlayer stacking structure,

212   corresponding with the thinner thickness of S-CN(0.1). While for the (001) peak, S-CN(0.1) also

213   exhibits much smaller intensity, suggesting the long-range polymerization along the in-plane

214   nanosheet is also suppressed, which is consistent with the existence the insert mesopore and

215   macropores as evidenced by the HRTEM images. Therefore, decreasing the amount of precursor

216   would not only promote inter-layer separation but also create pore in-plane, thus obtaining the holey

217   ultrathin g-C_3N_4 nanosheets.

218   EPR spectra were conducted to monitor the unpaired electrons, which should have a positive effect

219   on photocatalysis. From **Figure 2d**, all samples exhibit single Lorentzian lines, originated from the

carbon atoms in the pi-conjugated layer of g-C_3N_4. Compared with U-CN, S-CN(x) show a highly

enhanced EPR signal, suggesting the higher delocalization of the conjugated network. Moreover, S-

CN(0.1) exhibits the strongest concentration of unpaired electrons, which could be ascribed to the

synergy of sulfur-doping and nanosheet geometry. The g values were calculated to be 2.0051 of S-

CN(2.0) and 2.0046 of S-CN(0.1). The decreased g value for S-CN(0.1) would be assigned to the

increased delocalization and weak dipole-dipole electronic interaction [40].

Figure 3. High-resolution (a) C1s, (b) S2p and (d) N1s XPS spectra and (c) solid-state ^{13}C NMR of
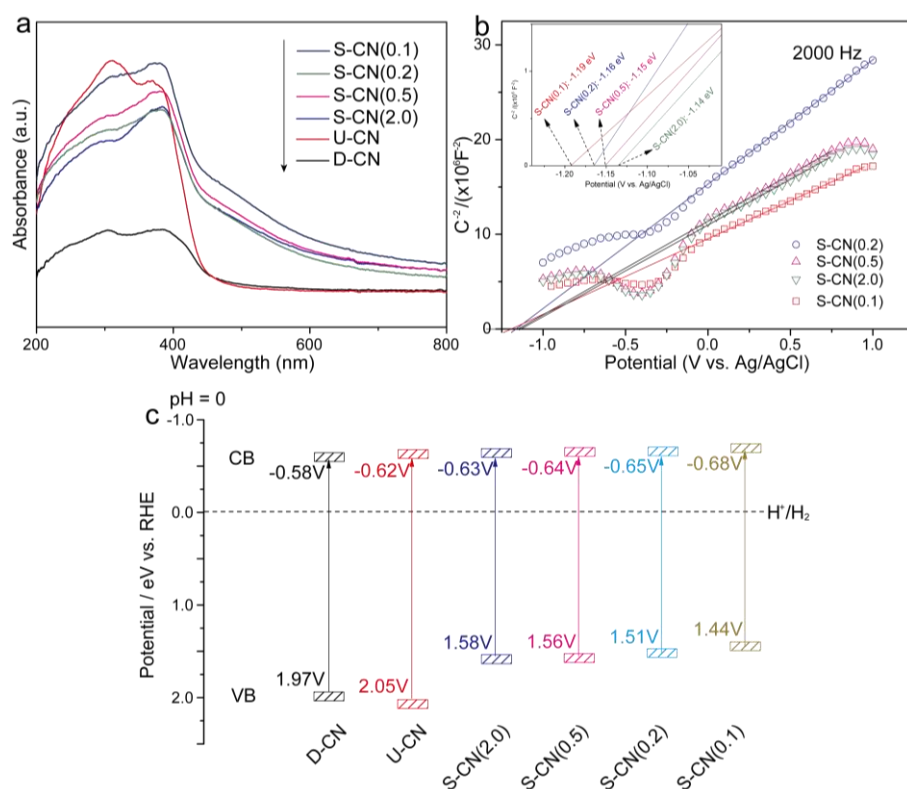
U-CN, S-CN(2.0) and S-CN(0.1).

The chemical states of S-CN(x) were investigated by XPS and shown in **Figure 3 and Figure S4**.

Survey XPS spectra confirm the existence of carbon, nitrogen, oxygen and sulfur elements. The O1s

peak centered at 532.5 eV is assigned to the adsorbed moisture. For the pristine U-CN, C1s spectra

12

(**Figure 3a**) display four peaks at 284.60, 285.87, 288.14 and 293.50 eV. The peak at 284.60 eV is featured as the adventitious carbon (C-C/C=C) and used to calibrate the current XPS spectra. The minor and dominant peaks at 293.50 and 288.14 eV are attributed to the sp^2-bonded C atoms in the heptazine heterocycle attached to the terminal $-NH_x$ (x = 1, 2) ($C-NH_x$) and the sp^2 hybridized C atoms in the heterocycle (N-C=N), respectively. In the case of S-CN(2.0), the C1s peak associated to N-C=N exhibits a slightly lower direction movement (about 0.10 eV) to 288.03 eV, demonstrating the improved electron density around carbon atom in the heterocycles. As the electronegativity of nitrogen atoms is much stronger than that of carbon atoms, the initial carbon atom in pristine U-CN acts as the electron donor. Therefore, when the electron density around carbon in S-CN(2.0) improves, the adjacent nitrogen atoms of N-C=N would be eliminated to form vacancy or be replaced by atoms with weaker electronegativity than that of nitrogen. As no existence of the defect-related absorption peaks like cyano group (C≡N) was seen in the FT-IR spectra (**Figure S5**), it clearly evidences the well-reserved characteristic heptazine framework, then demonstrating the anion doping of S-CN(2.0). For S-CN(0.1), the C1s peak of N-C=N further moves to lower binding energy at 287.96 eV, indicating more anion doping sites are induced by decreasing feeding amount. High resolution S_{2p} spectrum (**Figure 3b**) shows two peaks at 164.35 and 168.66 eV. The strong peak at 164.35 eV is attributed to the C-S bonds, which could be formed by substituting the sp^2 hybridized lattice nitrogen atom [41]. The solid ^{13}C nuclear magnetic resonance (NMR) spectra (**Figure 3c**) further evidence the sulfur-doped structure of S-CN(x). For U-CN, two peaks at 165.1 and 157.3 ppm are observed and assigned to the carbon of $C-NH_x$ and N-C=N in the heptazine, respectively. As a contrast, the peak corresponding to C-NHx splits with a shoulder peak at 162.7 ppm. This right-shifted shoulder peak suggests the significantly changed chemical states, with higher electron density around carbon of C-NH_x in the heptazine cycles. This peak would be attributed to carbon of S-C and evidences the

257 existence of sulfur dopants [42, 43]. Combining with the XPS, ^{13}C NMR spectra and elemental

258 analysis, it could conclude that sulfur atom substitutes the nitrogen in the heptazine cycles and forms

259 the sulfur doping structure. N1s spectra (**Figure 3d**) presence four peaks at 398.51, 399.78, 401.02

260 and 404.43 eV, attributing to the sp^2 hybridized N atoms in heterocycle (C-N=C), the sp^3 bridged N

261 atoms (H-N-C_3), amino functional groups (-NH_x) and pi electrons, respectively [44]. The ratio of sp^2

262 C-N=C bonds to the sum of sp^3 H-N-C_3 and C-N_x bonds is 3.69 in S-CN(0.1), much higher than 2.51

263 in S-CN(2.0). Since sp^3 band is a tetrahedral structure, it would play the major role in locally distorted

264 geometry for S-CN(2.0), corresponding with the curly morphology evidenced by HRTEM. As a

265 contrast, S-CN(0.1) with lower sp^3 contents imply long-range bending morphology. Therefore, the

266 curly multilayered stacking structure with reduced S_{BET} were observed for S-CN(2.0). Zeta potential

267 measurement of S-CN(2.0) and S-CN(0.1) were performed to evaluate the surface change induced by

268 sulfur doping and showed in **Figure S6**. It is clear that zeta potential of S-CN(0.1) (-30.3 mV) is more

269 negative than that of S-CN(2.0) (-26.5 mV), which would be favorable for the adsorption and

270 activation of H^+. The more negative charged surface might be attributed to the increased electron

271 delocalization caused by the sp^2 hybridization in S-CN(0.1) other than sp^3 hybridization in S-CN(2.0)

272 as proved by XPS measurement in **Figure 3** and higher concentration of unpaired electrons as
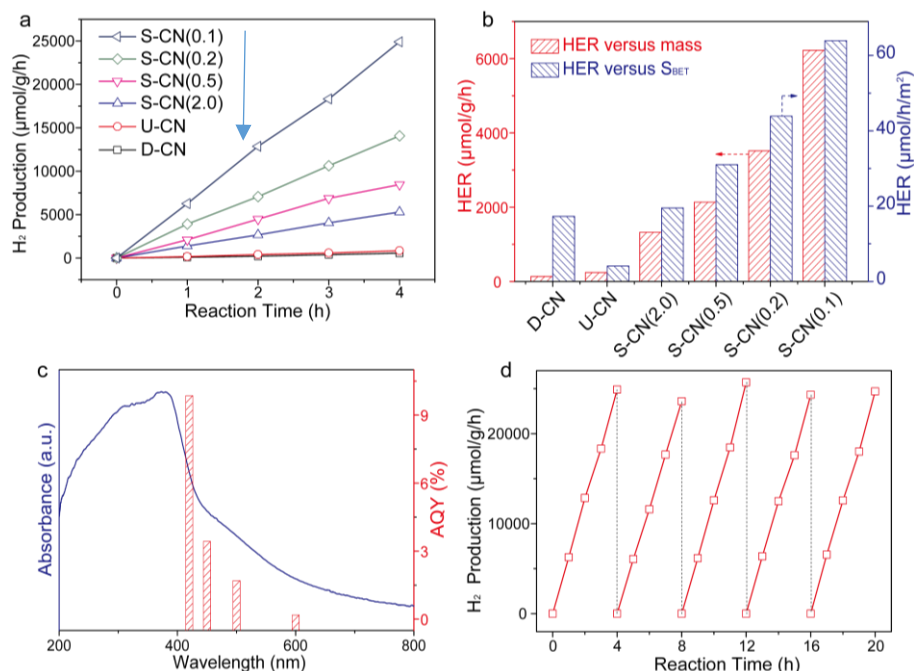
273 evidenced by EPR result (**Figure 2d**).

274

Figure 4. (a) UV-Vis diffuse reflectance spectra, (b) Mott-Schottky plots with its enlarged curves in the insert and (c) bandgap structure of different photocatalysts.

The optical properties were characterized by UV-DRS spectra. From **Figure 4a**, the photoabsorption is gradually red-shifted from 440 nm for U-CN to 478 nm for S-CN(2.0) and finally to 486 nm for S-CN(0.1), consistents with the color change from light yellow to deep yellow and brown yellow. The absorption around 400 nm and 500 nm were attributed to the π-π* and n-π* electronic transitions in the heptazine heterocycle and lone pairs of electrons [45]. The n-π* transitions in planar structure are usually forbidden but occurr in distorted polymeric units [46]. Compared with U-CN, an obviously enhanced photoabsorption was observed in the visible region for S-CN(x), which could be attributed to sulfur doping. Notably, the absorption boundary of S-CN(0.1) with thinner layer would have been blue-shifted due to the quantum confinement effect, however a red-shift exhibits in **Figure 4a**, demonstrating the significance of sulfur doping on visible absorption

promotion. The bandgap energy was calculated to be 2.67 eV of U-CN, 2.21 eV of S-CN(2.0) and 2.12 eV of S-CN(0.1) by the Tauc plots (**Figure S7**). The flat band was measured by the Mott-schottky plots (**Figure 4b**). The positive slope of S-CN(x) demonstrate the n-type semiconductor of g-C_3N_4. As the flat band for n-type semiconductor lies 0.1 eV below conduction band (CB) [47, 48], the corresponding CB positions were established respectively as -1.24 eV of S-CN(2.0), -1.25 eV of S-CN(0.5), -1.26 eV of S-CN(0.2) and -1.29 eV of S-CN(0.1) vs Ag/AgCl (pH = 7). Combining with the bandgap energy, the valance band position was calculated by $E_V = E_B + E_C$ (E_B, E_V and E_C respectively stand for the bandgap energy, the valence and conduction band energy level). The band positions with respect to RHE at pH = 0 are provided in **Figure 4c**, the narrowed bandgap energy for S-CN(0.1) ensures much wider photoabsorption and the more negative CB position would remain sufficient overpotential to drive photocatalytic hydrogen production.

Figure 5. (a) Photocatalytic hydrogen production ($\lambda > 420$ nm) over D-CN, U-CN and S-CN(x). (b) HER versus mass and surface area, (c) the apparent quantum yield on S-CN(0.1) versus

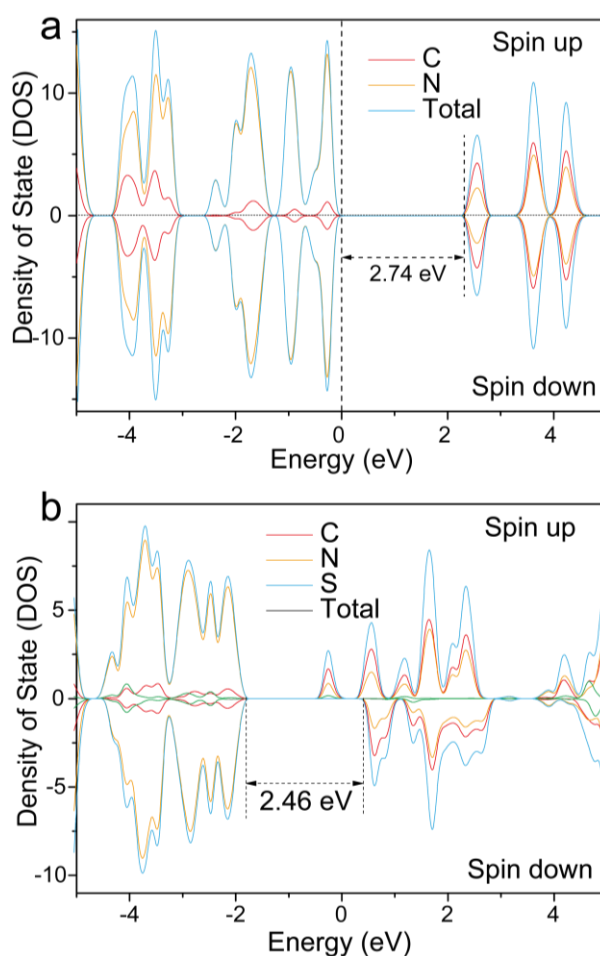wavelength, (d) photocatalytic reusability of S-CN(0.1).

3.2. Photocatalytic performance

Photocatalytic water splitting reactions under visible light ($\lambda > 420$ nm) irradiation were conducted to test the photocatalytic performance. Platinum (3 wt.%) and triethanolamine (TEOA) (10 vol.%) were used as the co-catalyst and sacrificial agent, respectively. Bulk and nanosheet g-C_3N_4 prepared from dicyandiamide and urea were evaluated as references. As shown in **Figure 5a**, dicyandiamide-derived bulk g-C_3N_4 (denoted as D-CN) exhibits a very low photocatalytic hydrogen evolution rate (HER) of 136.6 $\mu mol \cdot g^{-1} \cdot h^{-1}$, which is consistent with the literature and attributed to the insufficient photoabsorption, low S_{BET} and high charge recombination rate. Urea-derived g-C_3N_4 (U-CN) exhibits enhanced photocatalytic HER to 241.2 $\mu mol \cdot g^{-1} \cdot h^{-1}$, nearly 1.8 times higher than that of D-CN. Whereas the thiocyanuric acid-derived S-CN(2.0) performs dramatic improvement of photocatalytic HER to 1324.2 $\mu mol \cdot g^{-1} \cdot h^{-1}$, 5.5 times higher activity under visible light irradiation ($\lambda > 420$ nm) than U-CN. As the S_{BET} of S-CN(2.0) (67.8 m^2/g) is 1.2 times larger than U-CN (58.7 m^2/g), the 5.5 times photocatalytic enhancement could not only be attributed to the enlarged surface area, but also to the enhanced photoabsorption and charge separation as discussed below due to sulfur doping. When decreasing the amount of thiocyanuric acid, the as-prepared samples S-CN(x) exhibit gradually increased HER from 1324.2 to 6225.4 $\mu mol \cdot g^{-1} \cdot h^{-1}$, almost 4.7 times improvement and also higher than those reported previously (as shown in **Table S2**). Meanwhile, the amount of HER per unit surface area (**Figure 5b**) of S-CN(0.1) significantly improved to be 63.9 $\mu mol \cdot h^{-1} \cdot m^{-2}$, almost 3.3, 15.6 and 3.7 times improvement than that of S-CN(2.0) (19.5 $\mu mol \cdot h^{-1} \cdot m^{-2}$), U-CN (4.1 $\mu mol \cdot h^{-1} \cdot m^{-2}$) and D-CN (17.3 $\mu mol \cdot h^{-1} \cdot m^{-2}$). This boosted hydrogen production performance per unit surface area can only be ascribed to the more negative conduction band and narrowed bandgap resulted from

17

327   the sulfur-doped and ultra-thin two-dimensional structure. The apparent quantum yield (AQY)

328   reaches ca. 10% for S-CN(0.1) at 420 ± 10 nm. S-CN(0.1) (**Figure 5c**) also performs acceptable

329   stability under five cycles reuse (**Figure 5d**) with its photocatalytic HER stabilizes at ca. 6200 μmol·g⁻

330   ¹·h⁻¹. S-CN(0.1) still maintains nanosheet structure after photocatalytic reaction as shown in **Figure**

331   **S8**.

332

334   Figure 6. Density of states of (a) pristine g-C_3N_4 and (b) sulfur-doped g-C_3N_4.
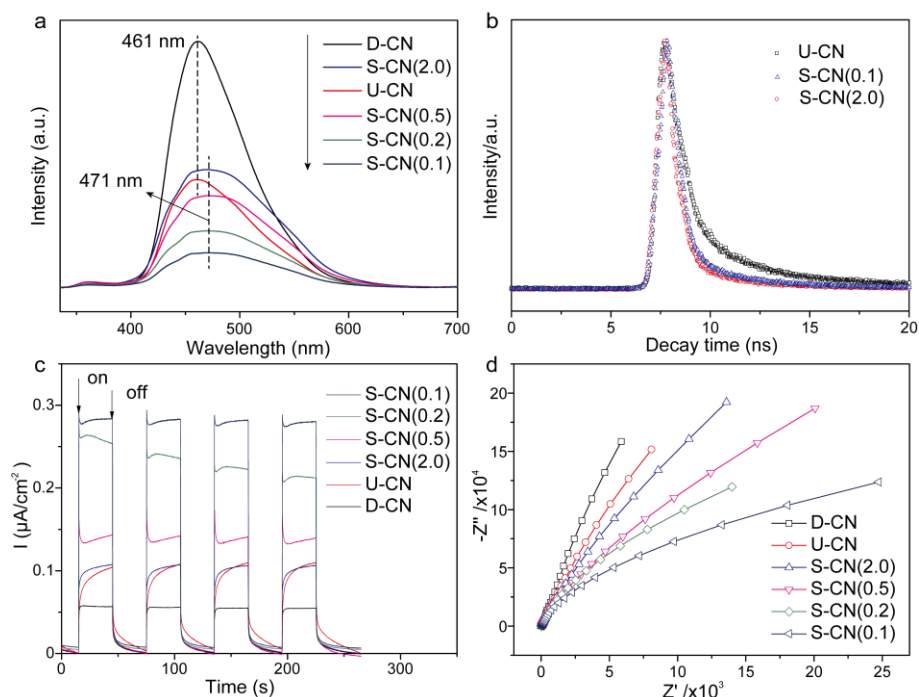
335

336   3.3. Role of sulfur and ultrathin holey nanosheet

337   Theoretical calculations were conducted to understand the boosted photocatalytic performances.

338   As shown in **Figure 6a**, the density of states (DOS) calculation results show the wide bandgap of

339   pristine g-C$_3$N$_4$ at 2.74 eV, being close to the bandgap energy (2.67 eV) established by the Tauc plots.

340   Meanwhile, carbon and nitrogen atoms primarily contribute to the conduction and valence band,

341   respectively, leading to numerous active sites for photocatalysis. As for the sulfur-doped g-C$_3$N$_4$ (S-

342   C$_3$N$_4$), the substitution of nitrogen with sulfur in the heptazine would modify the valence band of g-

343   C$_3$N$_4$. From **Figure 6b**, density of states exhibit an obvious left-shift to lower energy, which is

344   consistent with the movement of the bandgap position of S-CN(x) as illustrated in **Figure 4c**.

345   Meanwhile, the bandgap energy was calculated as 0.49 eV (spin-up) and 2.46 eV (spin-down) after

346   sulfur-doping, much lower than that of pristine g-C$_3$N$_4$. Taking into account the real bandgap of 2.12

347   to 2.21 eV of S-CN(x) measured by UV-Vis spectra, the 2.46 eV is the bandgap responsive for visible

348   photon absorption. Moreover, the doping energy in **Figure 6b** at -0.25 eV (spin-up) consists little

349   sulfur, demonstrating that sulfur directly makes little contribution to the narrowed bandgap. As the

350   narrowed bandgap could originate either from the doping energy level or from the distorted crystal

351   structure. Based on the partial DOS analysis, the reduced bandgap is likely due to the distortion of

352   the crystal structure caused by sulfur doping. The distorted structure is corresponding with the

353   distorted interlayer structure as proved by the XRD.

354

Figure 7. (a) PL spectra, (b) time-resolved PL spectra, (c) photocurrent responses versus time and (d) EIS plots of different photocatalysts.

Steady-state photoluminescence (PL) spectra were performed to evaluate the charge recombination rate (**Figure 7a**). A stronger PL intensity usually refers to a higher charge recombination rate. The lowest PL peak intensity of S-CN(0.1) indicates the highest charge separation efficiency, which is assigned not only to the morphological evolution to ultrathin holey nanosheets, but also to the sulfur dopants serving as the trapping sites for photogenerated charge carriers. Meanwhile, compared with D-CN and U-CN, a red-shifted PL emission wavelength at 471 nm for S-CN(x) was observed, which is consistent with the narrowed bandgap, originated from the sulfur doping as evidenced by the DOS calculation. To understand the charge transfer behavior of photogenerated charge carriers, time-resolved PL spectra were acquired and fitted by the two-exponential decay. It can be seen from **Figure 7b** that the fluorescent intensity of both S-CN(2.0) and S-CN(0.1) decay exponentially. Both S-CN(2.0) and S-CN(0.1) exhibit a similar band-to-band emission character. Compared with S-CN(2.0),

20

370   the much more delayed emission peaks of S-CN(0.1) indicates much slower fluorescent decay

371   kinetics and suppressed recombination efficiency. The fitted results give two radiative lifetimes. For

372   both S-CN(2.0) and S-CN(0.1), the amount of the short-lived carrier is dominant as a result of the

373   rapid charge recombination. Notably, the lifetime of short-lived carrier (0.64 ns, 92%) for S-CN(0.1)

374   is much longer than that of S-CN(2.0) (0.53 ns, 91%), and the long-lived carrier (4.65 ns, 8%) for S-

375   CN(0.1) is also longer than that of S-CN(2.0) (4.25 ns, 9%). These results suggest that the sulfur

376   doping atoms in S-CN(0.1) could act as the shallow trapping sites to prolong lifetime of charge carrier,

377   [49-51] which is in favor of the carrier trapping by the reactant and retarding the charge recombination.

378   Photocurrent density (**Figure 7c**) further proves the more efficient charge separation. S-CN(0.1)

379   exhibits the highest photocurrent density at 0.28 $\mu A/cm^2$, almost 2.6 and 5.1 times higher than that of

380   S-CN(2.0) and D-CN. Electrochemical impedance spectroscopy (EIS) Nyquist plots (**Figure 7d**)

381   present the smallest radius of S-CN(0.1) than the others, indicating a much smaller resistance and

382   being beneficial to the interfacial charge transfer.

383   Based on the above results, the significant improvement of photocatalytic performance is realized.

384   Through controllable thermolysis, ultrathin holey g-C_3N_4 nanosheets were prepared and beneficial to

385   expose much more accessible surface to absorb and active H^+ as proved by more negative zeta

386   potential. Moreover, the more negative CB position performs much stronger photoreduction ability

387   and the enhanced charge separation efficiency were also promoted as evidenced by the PL spectra,

388   photocurrent response and theoretical calculations. As a result, the boosted photocatalytic

389   performance is ascribed to the synergy of the ultra-thin holey nanosheet morphology and the

390   electronic modification induced by sulfur doping.

391   3.4. Universal method for various precursors

392   Besides thiocyanuric acid, other common precursors including melamine, dicyanamide, thiourea

and urea were applied to investigate the universality of this reliable method for structural engineering. When using melamine as the precursor, the yield of g-C_3N_4 gradually decreases and S_{BET} gradually increases as with the decreased feeding amount (**Figure S9a-b**). Notably, when the amount of melamine was below 0.5 g, the yield and S_{BET} of g-C_3N_4 both experienced a drastic change, attributing to the dominant role of gaseous polymerization. Further decreasing the amount of melamine below 0.2 g generates no products, ascribed to the complete sublimation and decomposition of melamine. For other general used precursors, although drastic self-decomposition occurs, it still follow the same way to optimize the textural properties as shown in **Figure S9a-b**. The differences among those precursors result from their unique properties, including the polymerization degree and decomposition. It is clear that the S_{BET} of g-C_3N_4 could be regulated universally by subtly decreasing the feeding amount.

Corresponding to the change of S_{BET}, the morphology gradually changed from bulk to nanosheets with the feeding amount decreasing even from melamine precursor. Conventional g-C_3N_4 prepared from melamine is usually dense and bulk (**Figure S10a**). While with less amount of melamine, the morphology gradually exhibits an evolution from bulk of M-CN(5.0) to nanosheets of M-CN(0.2) (**Figure S10b-c**). In the case of urea, decreasing the feeding amount from 10.00 to 2.00 g, g-C_3N_4 exhibits an obvious structural evolution from curly nanosheets to the decurved nanosheets or nanomesh (**Figure S10d-f**), corresponding to the increased S_{BET} from 58.7 to 177.3 m^2/g, almost 3 times improvement. As a contrast, g-C_3N_4 obtained from thiourea exhibits mesoporous g-C_3N_4 aggregates with more feeding amount (**Figure S10g-i**), but nanosheets can also be obtained after minimizing the feeding amount, with the corresponding S_{BET} dramatically increasing from 19.6 to 81.3 m^2/g. In the case of dicyanamide-derived g-C_3N_4, decreasing the feeding amount can also reach enlarged S_{BET} from 7.9 to 47.2 m^2/g.

4. Conclusion

In summary, sulfur-doped holey g-C_3N_4 nanosheets were prepared through subtly controlling the amount of thiocyanuric acid precursor. Thin thickness from 2.4 nm of S-CN(2.0) to 0.8 nm of S-CN(0.1) and the corresponding enlarged S_{BET} were observed, which is beneficial to expose more accessible surface to absorb and active H^+. XPS and ^{13}C NMR spectra evidenced the sulfur doping topology, resulting in greatly promoted visible light absorption. The conduction band was thus shifted from 0.62 V of U-CN to 0.63 V of S-CN(2.0) and 0.68 V of S-CN(0.1), providing stronger photoreduction ability. As a result, photocatalytic hydrogen production was realized from UV till 600 nm, with the apparent quantum yield reaching 10 % at 420 nm and 0.18% at 600 nm. The optimized hydrogen evolution rate ($\lambda > 420$ nm) reaches 6225.4 $\mu mol \cdot g^{-1} \cdot h^{-1}$, almost 45 times higher than the pristine bulk g-C_3N_4, attributed to the synergy of the ultrathin holey nanosheet and sulfur doping structure. This work highlights the importance of feeding amount and provides a promising and universal pathway to simultaneously regulate the nanostructural and electronic structure of g-C_3N_4 in one-step thermolysis.

CRediT authorship contribution statement

Lei Luo: Design, Methodology, Investigation, Data collection, Drafting. **Zhuyu Gong:** Data collection, Investigation. **Jiani Ma:** Data analysis, Result discussion, Resources. **Keran Wang:** Investigation. **Haixing Zhu:** Investigation. **Keyan Li:** Results discussion **Lunqiao Xiong:** Results discussion, Revision. **Xinwen Guo:** Supervision, Resources, Review, Editing. **Junwang Tang:** Overall supervision, Resources, Review, Editing.

Declaration of Competing Interest

The authors reported no declarations of interest.

Acknowledgements

References

[1] Wang, Y., A. Vogel, M. Sachs, R.S. Sprick, L. Wilbraham, S.J.A. Moniz, R. Godin, M.A. Zwijnenburg, J.R. Durrant, A.I. Cooper, and J. Tang. *Nature Energy*, **2019**, 4, 746.

[2] Jourshabani, M., B.-K. Lee, and Z. Shariatinia. *Applied Catalysis B: Environmental*, **2020**, 276, 119157.

[3] Wang, Q. and K. Domen. *Chemical Reviews*, **2020**, 120, 919.

[4] Gao, Q., J. Xu, Z. Wang, and Y. Zhu. *Applied Catalysis B: Environmental*, **2020**, 271, 118933.

[5] Fu, J., Q. Xu, J. Low, C. Jiang, and J. Yu. *Applied Catalysis B: Environmental*, **2019**, 243, 556.

[6] Chen, X., R. Shi, Q. Chen, Z. Zhang, W. Jiang, Y. Zhu, and T. Zhang. *Nano Energy*, **2019**, 59, 644.

[7] Wang, T., C. Nie, Z. Ao, S. Wang, and T. An. *Journal of Materials Chemistry A*, **2020**, 8, 485.

[8] Zhou, C., R. Shi, L. Shang, L.-Z. Wu, C.-H. Tung, and T. Zhang. *Nano Research*, **2018**, 11, 3462.

[9] Zeng, Z., H. Yu, X. Quan, S. Chen, and S. Zhang. *Applied Catalysis B: Environmental*, **2018**, 227, 153.

[10] Liu, C., H. Huang, W. Cui, F. Dong, and Y. Zhang. *Applied Catalysis B: Environmental*, **2018**, 230, 115.

462   [11] Luo, L., K. Li, A. Zhang, H. Shi, G. Zhang, J. Ma, W. Zhang, J. Tang, C. Song, and X. Guo.

463   *Journal of Materials Chemistry A*, **2019**.

464   [12] Lin, L., Z. Yu, and X. Wang. *Angewandte Chemie International Edition*, **2019**, 58, 6164.

465   [13] Wang, K., Y. Li, J. Li, and G. Zhang. *Applied Catalysis B: Environmental*, **2020**, 263, 117730.

466   [14] Zhang, D., Y. Guo, and Z. Zhao. *Applied Catalysis B: Environmental*, **2018**, 226, 1.

467   [15] Luo, L., J. Ma, H. Zhu, and J. Tang. *Nanoscale*, **2020**, 12, 7339.

468   [16] Tan, C., X. Cao, X.J. Wu, Q. He, J. Yang, X. Zhang, J. Chen, W. Zhao, S. Han, G.H. Nam, M.

469   Sindoro, and H. Zhang. *Chem Rev*, **2017**, 117, 6225.

470   [17] Dong, R., T. Zhang, and X. Feng. *Chemical Reviews*, **2018**, 118, 6189.

471   [18] Wang, Y., H. Suzuki, J. Xie, O. Tomita, D.J. Martin, M. Higashi, D. Kong, R. Abe, and J. Tang.

472   *Chemical Reviews*, **2018**, 118, 5201.

473   [19] Yuan, Y.-J., Z. Shen, S. Wu, Y. Su, L. Pei, Z. Ji, M. Ding, W. Bai, Y. Chen, Z.-T. Yu, and Z. Zou.

474   *Applied Catalysis B: Environmental*, **2019**, 246, 120.

475   [20] Xiao, Y., G. Tian, W. Li, Y. Xie, B. Jiang, C. Tian, D. Zhao, and H. Fu. *Journal of the American

476   Chemical Society*, **2019**, 141, 2508.

477   [21] Papailias, I., N. Todorova, T. Giannakopoulou, N. Ioannidis, N. Boukos, C.P. Athanasekou, D.

478   Dimotikali, and C. Trapalis. *Applied Catalysis B: Environmental*, **2018**, 239, 16.

479   [22] Cui, L., Y. Liu, X. Fang, C. Yin, S. Li, D. Sun, and S. Kang. *Green Chemistry*, **2018**, 20, 1354.

480   [23] Wang, Z., C. Li, and K. Domen. *Chemical Society Reviews*, **2019**, 48, 2109.

481   [24] Liu, G., P. Niu, C. Sun, S.C. Smith, Z. Chen, G.Q.M. Lu, and H.-M. Cheng. *Journal of the

482   American Chemical Society*, **2010**, 132, 11642.

483   [25] Huang, Y., D. Li, Z. Fang, R. Chen, B. Luo, and W. Shi. *Applied Catalysis B: Environmental*,

484   **2019**, 254, 128.

485 [26] Gao, H., R. Cao, S. Zhang, H. Yang, and X. Xu. *ACS Applied Materials & Interfaces*, **2018**, 11,

486   2050.

487 [27] Che, W., W. Cheng, T. Yao, F. Tang, W. Liu, H. Su, Y. Huang, Q. Liu, J. Liu, F. Hu, Z. Pan, Z.

488   Sun, and S. Wei. *Journal of the American Chemical Society*, **2017**, 139, 3021.

489 [28] Fang, J., H. Fan, M. Li, and C. Long. *Journal of Materials Chemistry A*, **2015**, 3, 13819.

490 [29] Ong, W.J., L.-L. Tan, Y.H. Ng, S.-T. Yong, and S.-P. Chai. *Chemical Reviews*, **2016**, 116, 7159.

491 [30] Chu, K., Q.-q. Li, Y.-p. Liu, J. Wang, and Y.-h. Cheng. *Applied Catalysis B: Environmental*, **2020**,

492   267, 118693.

493 [31] Fang, Y., X. Li, Y. Wang, C. Giordano, and X. Wang. *Applied Catalysis B: Environmental*, **2020**,

494   268, 118398.

495 [32] Wang, X., K. Maeda, A. Thomas, K. Takanabe, G. Xin, J.M. Carlsson, K. Domen, and M.

496   Antonietti. *Nature Materials*, **2009**, 8, 76.

497 [33] Li, Y., M. Yang, Y. Xing, X. Liu, Y. Yang, X. Wang, and S. Song. *Small*, **2017**, 13, 1701552.

498 [34] Dong, G., K. Zhao, and L. Zhang. *Chemical Communications*, **2012**, 48, 6178.

499 [35] Zhang, R., A. Khalizov, L. Wang, M. Hu, and W. Xu. *Chemical Reviews*, **2012**, 112, 1957.

500 [36] Li, Y., R. Jin, Y. Xing, J. Li, S. Song, X. Liu, M. Li, and R. Jin. *Advanced Energy Materials*,

501   **2016**, 6, 1601273.

502 [37] Jiang, L., J. Li, K. Wang, G. Zhang, Y. Li, and X. Wu. *Applied Catalysis B: Environmental*, **2020**,

503   260, 118181.

504 [38] Merschjann, C., S. Tschierlei, T. Tyborski, K. Kailasam, S. Orthmann, D. Hollmann, T. Schedel-

505   Niedrig, ArneThomas, and S. Lochbrunner. *Advanced Materials*, **2015**, 27, 7993.

506 [39] Rahman, M.Z. and C.B. Mullins. *Acc Chem Res*, **2019**, 52, 248.

507 [40] Zhang, G., M. Zhang, X. Ye, X. Qiu, S. Lin, and X. Wang. *Advanced Materials*, **2014**, 26, 805.

508 [41] Wang, K., Q. Li, B. Liu, B. Cheng, W. Ho, and J. Yu. *Applied Catalysis B: Environmental*, **2015**,

509   176-177, 44.

510 [42] Cui, Y., M. Li, H. Wang, C. Yang, S. Meng, and F. Chen. *Separation and Purification Technology*,

511   **2018**, 199, 251.

512 [43] Afonin, A.V., D.V. Pavlov, A.I. Albanov, O.g.A. Tarasova, and N.A. Nedolya. *Magnetic*

513   *Resonance in Chemistry*, **2013**, 51, 414.

514 [44] Martin, D.T., K. Qiu, S.A. Shevlin, A.D. Handoko, X. Chen, Z. Guo, and J. Tang. *Angewandte*

515   *Chemie International Edition*, **2014**, 126, 9394.

516 [45] Wang, Y., M.K. Bayazit, S.J.A. Moniz, Q. Ruan, C.C. Lau, N. Martsinovich, and J. Tang. *Energy*

517   *& Environmental Science*, **2017**, 10, 1643.

518 [46] Jorge, A.B., D.J. Martin, M.T.S. Dhanoa, A.S. Rahman, N. Makwana, J. Tang, A. Sella, F. Corà,

519   S. Firth, J.A. Darr, and P.F. McMillan. *The Journal of Physical Chemistry C*, **2013**, 117, 7178.

520 [47] Battula, V.R., S. Kumar, D.K. Chauhan, S. Samanta, and K. Kailasam. *Applied Catalysis B:*

521   *Environmental*, **2019**, 244, 313.

522 [48] Sun, S., W. Wang, D. Li, L. Zhang, and D. Jiang. *ACS Catalysis*, **2014**, 4, 3498.

523 [49] Fitzmorris, B.C., G.K. Larsen, D.A. Wheeler, Y. Zhao, and J.Z. Zhang. *The Journal of Physical*

524   *Chemistry C*, **2012**, 116, 5033.

525 [50] Shi, H., S. Long, S. Hu, J. Hou, W. Ni, C. Song, K. Li, G.G. Gurzadyan, and X. Guo. *Applied*

526   *Catalysis B: Environmental*, **2019**, 245, 760.

527 [51] Ruan, Q., T. Miao, H. Wang, and J. Tang. *Journal of the American Chemical Society*, **2020**, 142,

528   2795.

529